Composites Part B 263 (2023) 110835

Contents lists available at ScienceDirect

Composites Part B

journal homepage: www.elsevier.com/locate/compositesb

Flexible composite films with enhanced piezoelectric properties for energy harvesting and wireless ultrasound-powered technology

Floriana Craciun [a,*], Francesco Cordero [a], Elisa Mercadelli [b], Nikola Ilic [c], Carmen Galassi [b], Carlo Baldisserri [b], Jelena Bobic [c], Paola Stagnaro [d], Giovanna Canu [e], Maria Teresa Buscaglia [e], Adis Dzunuzovic [c], Mirjana Vijatovic Petrovic [c]

[a] CNR-ISM, Istituto di Struttura della Materia, Area della Ricerca di Tor Vergata, Via del Fosso del Cavaliere, 100, Rome, Italy
[b] CNR-ISSMC, Institute of Science, Technology and Sustainability for Ceramics (formerly ISTEC-CNR), Via Granarolo 64, Faenza, Italy
[c] Institute for Multidisciplinary Research, University of Belgrade, Kneza Viseslava 1, Belgrade, Serbia
[d] CNR-SCITEC, Istituto di Scienze e Tecnologie Chimiche "Giulio Natta", Via de Marini 6, Genoa, Italy
[e] CNR-ICMATE, Istituto di Chimica della Materia Condensata e di Tecnologie per l'Energia, Consiglio Nazionale delle Ricerche, Via de Marini 6, Genoa, Italy

ARTICLE INFO

Handling Editor: Prof. Ole Thomsen

Keywords:
Polymer-matrix composites
Multifunctional composites
Electrical properties
Mechanical properties

ABSTRACT

In the last years, ultrasound energy harvesting has emerged as the most promising technique for wireless power supply of implanted medical devices. These devices require flexible piezoelectric materials with high piezoelectric response in the ultrasonic range. Here we report on bio-compatible NBT-BT/PVDF flexible composites, with variable filler content up to 50 vol%, prepared by a properly designed and optimized process, which incorporates in a complex connectivity pattern fully sintered NBT-BT crystalline powders in a PVDF matrix. The dielectric constant of the flexible composites increased from 10 of pure PVDF polymer to 110 of composite films with 50 vol% NBT-BT content, while the high frequency piezoelectric d_{33} constant increased from 0.2 pC/N to 33 pC/N for the same samples. The composite with 50 vol% NBT-BT exhibits the figure of merit for the harvested ultrasound energy $d_{33}g_{33} \cong 1.54 \times 10^{-12}$ m^3/J, which is comparable to the figure of merit for the NBT-BT piezoelectric ceramic (1.8×10^{-12} m^3/J) and higher than other reported results for random composites. Based on these results, this study provides an easy method to fabricate random flexible piezoelectric composites with enhanced high frequency piezoelectric response and high energy density harvested from an ultrasound source.

1. Introduction

In the last years different wireless energy harvesting solutions have been proposed for the reliable and stable powering of implanted biomedical devices (IBDs) [1]. The research in this field was boosted by the necessity to solve the well-known weak point of IBDs, that is, electrochemical batteries being needed to power the device. Indeed, since batteries' duration is short, more surgical operations should be done on patients to change the batteries, resulting into higher infection probabilities. Besides, wireless energy harvesting devices would be useful for other important applications, such as wireless stimulation of stem cells for nerve growth [2,3], improved wound medication [4] etc. Therefore, an important amount of research has been dedicated to promote the development of wireless energy harvesting devices for biomedical applications. Unlike energy harvesting from environmental sources, this technique relies on a stable source of energy. During the last years, different wireless energy harvesting solutions have been explored, including electromagnetic field, inductive power transfer and ultrasonic energy transfer [1]. Compared to the electromagnetic field, the ultrasound field radiation is more safe and less attenuated in the tissues. Moreover, it can be better focused due to the smaller wavelength. Therefore, ultrasound energy harvesting is an attractive technique for implanted devices powering. For efficient energy conversion, piezoelectric ceramics are the materials of choice in these devices. In addition to their non-toxicity and bio-compatibility, there are other requirements which are imposed on the materials for an efficient design: the piezoelectric ceramics must have a high figure of merit (FOM), the latter being defined as the product of their piezoelectric charge (d_{33}) and piezoelectric voltage (g_{33}) constants. Although pure piezoelectric ceramics have high d_{33}, their g_{33} constant (which is the d_{33}/ε_{33} ratio,

* Corresponding author.
E-mail address: floriana.craciun@ism.cnr.it (F. Craciun).

https://doi.org/10.1016/j.compositesb.2023.110835
Received 27 February 2023; Received in revised form 19 May 2023; Accepted 6 June 2023
Available online 8 June 2023

where ε_{33} is the dielectric constant) is generally low, due to the high dielectric constant. Along with other advantages that will be further discussed, piezoelectric ceramic/polymer composites can have higher FOM than ceramics, due to the low dielectric constant of the polymer. Another requirement is related to the sound transmission at the interface. A large mismatch between the acoustic impedance of the tissue and that of the implanted material leads to reflection of ultrasound and loss of energy transfer efficiency. Taking into account that piezoelectric ceramics have high acoustic impedance (~30 MRayls), whereas the tissues have much lower acoustic impedance (~1.5 MRayls), a piezoelectric material with lower acoustic impedance than that of piezoceramics should be chosen. A further requirement concerns the minimization of energy losses. The largest part of power losses for ultrasound-based implants is due to the divergence of the acoustic beam, which is related to the ratio of the ultrasound source diameter to the wavelength. For an efficient energy harvesting in a small volume, the ultrasound beam should be focused. Moreover, short-wavelength high-frequency ultrasound allows excellent spatial resolution by making it possible to focus the power on millimeter-sized regions. By summarizing these requirements, flexible bio-compatible piezoelectric composites with high d_{33} and g_{33} piezoelectric coefficients (i.e. high FOM) at high frequencies should be used for efficient wireless ultrasonic powering of IBDs.

In a piezoelectric composite the d_{33} charge coefficient depends not only on the filler's volume fraction but also on the connectivity of the phases [5]. A common type is the 0–3 composite, where the filler phase particles are randomly dispersed inside the polymer matrix, which is connected along all three directions. While 0–3 composites are easy to prepare, at low volume fraction of ceramic filler the electric field remains confined in the polymer, leading to poor dielectric and piezoelectric properties. Alternatively, 1–3 composites, comprising aligned ceramic bars inside the polymer matrix, can have high functional properties [5] but they require a much more difficult fabrication method. Different results have been reported on these systems [5–13]. To ensure easy industrial scalability of the production process of piezoelectric composites, simple production routes should be pursued as far as possible. Thus, in this study we have investigated random 0–3 composites which can be prepared by a simple process.

Depending on the intended application, the ceramic fillers normally employed in piezoelectric composites range from fine powders with dimensions from a few tens of nm to coarser powders up to a few hundreds of nm. It is well known that the ferroelectric properties are strongly decreased in nanoparticles with dimensions smaller than a few tens of nanometers [14]. In fact, the reduction of functional properties occurs when the grain size decreases already below 1 μm [14]. This is due to the reduced contribution of the ferroelectric domain walls. Indeed, domain walls mobility depends on the size of the confining region and it is maximum in micrometer-sized grains, where complex domain structures are observed. These domain structures become simpler with decreasing grain size and, below ~200 nm only simple configurations are observed. In these particles the domain wall motion is strongly hampered.

Therefore, in the fabrication of the composites we employed fully sintered and densified ceramic samples with well grown crystallites of micrometric dimension, which were crushed, milled, sieved and annealed, before mixing with the polymer. Thus, in our case the ceramic filler phase is made of particles which are good piezoelectrics in their own right, and do not require any further treatment except for poling after embedding in the polymer matrix. The issue of poling of the composite will be treated in Section 2.

In this paper we propose a new strategy to design high-performance flexible piezocomposites by employing fully sintered lead-free NBT-BT ceramic filler particles distributed in the PVDF polymer matrix. These composites display enhanced high frequency piezoelectric properties which make them very attractive for wireless ultrasound-powered medical implants. The so-obtained structure exhibits a clear high-frequency electromechanical behavior, responding with a synchronous electrical signal to an applied mechanical deformation in the ultrasound range.

2. Experimental procedure

2.1. Preparation of NBT-BT filler powders and flexible composite films

For the synthesis of the filler powders of $0.94[(Na_{0.5}Bi_{0.5})TiO_3]-0.06BaTiO_3$ (NBT-BT) by the solid state route, stoichiometric amounts of Na_2CO_3 (Merck), Bi_2O_3 (Aldrich), TiO_2 (Degussa) and $BaCO_3$ (Merck) have been first mixed by ball milling in ethanol, then dried and sieved. The detailed process is described in Ref. [13]. After calcination at 800 °C for 1 h, the powder was ball milled, then pressed in discs and sintered at 1150 °C for 30 min. After cooling, the sintered pellets were crushed into powder that was annealed at 700 °C and sieved at 40 μm.

For the preparation of composite samples, the NBT-BT powder was mixed with PVDF powder (Alfa Aesar) in four different proportions: 30, 35, 40 and 50 vol% ceramic powder. The powders were mixed in isopropanol under sonication and the mixture was then dried in a stove at 60 °C. The piezocomposite films were obtained by hot-pressing the powders (see sketch in Fig. 1), following a standardized procedure consisting of heating up to 190 °C, holding at the maximum temperature under a pressure of 5 MPa for 10 min, and then releasing the pressure as the temperature had decreased below 160 °C. The nomenclature of the samples corresponds to the content of filler: NBT-BT/PVDF 30, NBT-BT/PVDF 35, NBT-BT/PVDF 40 and NBT-BT/PVDF 50.

2.2. Poling of composite films

For poling (as well as for the dielectric and piezoelectric characterization), silver electrodes (~6 mm in diameter) were applied on the film surfaces with PEMCO silver paint. Polarization of the samples was achieved at 50 kV/cm. The DC electric field was applied for 40 min on the sample placed in a silicone oil bath at 135 °C. The sample has been subsequently cooled down to 50 °C, before removing the poling field.

2.3. Characterization techniques

The structure of NBT-BT powders was analyzed by X-ray diffraction (XRD) by using a Bruker D8 Advance X-ray Diffractometer and Rigaku MiniFlex 600 instrument. The morphology of particles was investigated by scanning electron microscopy (SEM) with a LEO 1450VP SEM microscope The morphology of composite films was imaged using a Tescan VEGA TS 5130 MM scanning electron microscope. The images have been taken on film surface and on the cross section (the latter obtained by cryo-fracture of the samples).

Fourier-transform infrared (FTIR) spectroscopy of composites was performed with a PerkinElmer Spectrum Two™ FTIR spectrometer operating in the attenuated total reflectance (ATR) mode. Absorbance spectra were collected over the 4000-400 cm^{-1} wavenumber range.

The crystallinity degree, X_C, was obtained from measurements with differential scanning calorimetry (DSC), by using a Mettler DSC 821 instrument. Two measurements per sample were made by heating from room temperature up to 220 °C in nitrogen with a heating rate of 10 °C/min. The crystallinity degree was calculated as described in Refs. [13,15].

Complex dielectric permittivity measurements were made with an HP4284A meter fitted with a four wire probe in the 150–410 K temperature range at five selected frequencies between 0.2 and 200 kHz, and at room temperature over the 100 Hz - 1 MHz frequency range. A modified Linkam HFS600E-PB4 stage has been employed for heating/cooling ramps.

Piezoelectric measurements at ultrasound frequency were performed on poled samples with an assembled experimental set-up, basically similar to those used in other works [16–18]. This includes a frequency generator, an amplifier, a vibrating device, an oscilloscope and a data

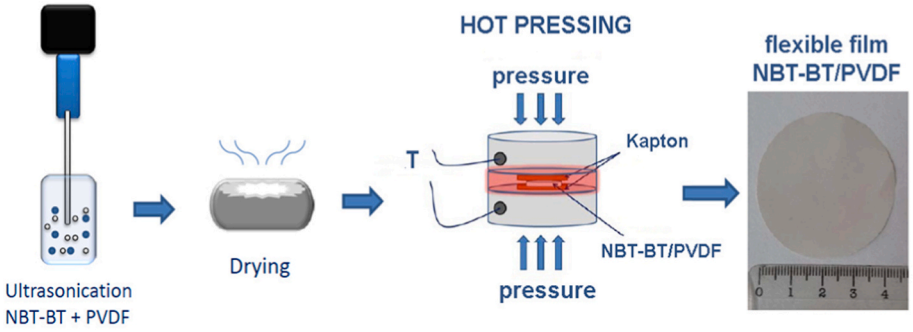

Fig. 1. Schematics for the preparation procedure of NBT-BT/PVDF composites.

acquisition system. The main differences are imposed by the specific frequency range of the measurement, in the MHz domain, while other systems work in the Hz domain (up to 50 Hz) [16–18]. Therefore, instead of using a classical electromechanical vibrator, which works at low frequency, we use a piezoceramic transducer assembled in a piezoelectric probe device [19], which sends an acoustical signal at 2 MHz in the piezoelectric composite film (which was previously poled in a high electric field, as described in Section 2.2). The synchronous electrical response of the composite film (at 2 MHz) is measured by the oscilloscope. We use a burst-type electrical signal to drive the probe transducer. This is generated by a Wavetek function generator and then amplified by a radio frequency power amplifier.

Piezoelectric resonance measurements were performed on poled samples with a HP 4194A impedance analyzer by applying a 1 V/mm amplitude AC signal.

Anelastic measurements were performed on strip samples (~30 mm long) which have been suspended on two thin thermocouple wires in vacuum and electrostatically excited in their flexural modes. The measurements of the complex dynamic Young's modulus ($Y=Y' + iY''$) in the kHz frequency range have been carried out in the 130–410 K temperature range with the free flexural resonance method [20].

3. Results and discussion

3.1. Structural characterization of active phase powders and composite films

The XRD pattern reported in Fig. 2 a) (bottom spectrum) shows that after calcination the powder is mainly composed by NBT-BT (with 4% BT, JCPDS 74–9529), crystallized in the rhombohedral structure with space group *R3c*, along with traces of un-reacted BT phase (JCPDS 66–0829). Clearly the desired structure has not been reached at this temperature. After sintering the NBT-BT ceramic at 1150 °C, the powder obtained by crushing and annealing was again investigated by XRD. The obtained pattern (upper spectrum in Fig. 2 a) corresponds to the desired NBT-BT structure (JCPDS 63–0299), evidencing both the presence of the tetragonal phase and its coexistence with the rhombohedral phase, which is the hallmark of the composition with 6% BT, at which the NBT-BT solid-solution materials attain the maximum of their functional properties [21]. The NBT-BT powders were morphologically characterized by SEM. Fig. 2 b) displays a SEM image of NBT-BT calcined powder, where aggregates of nanoparticles can be observed. Fig. 2 c) shows a SEM image of sintered and crushed NBT-BT powder, where well-formed crystallites with micrometer dimensions are observed.

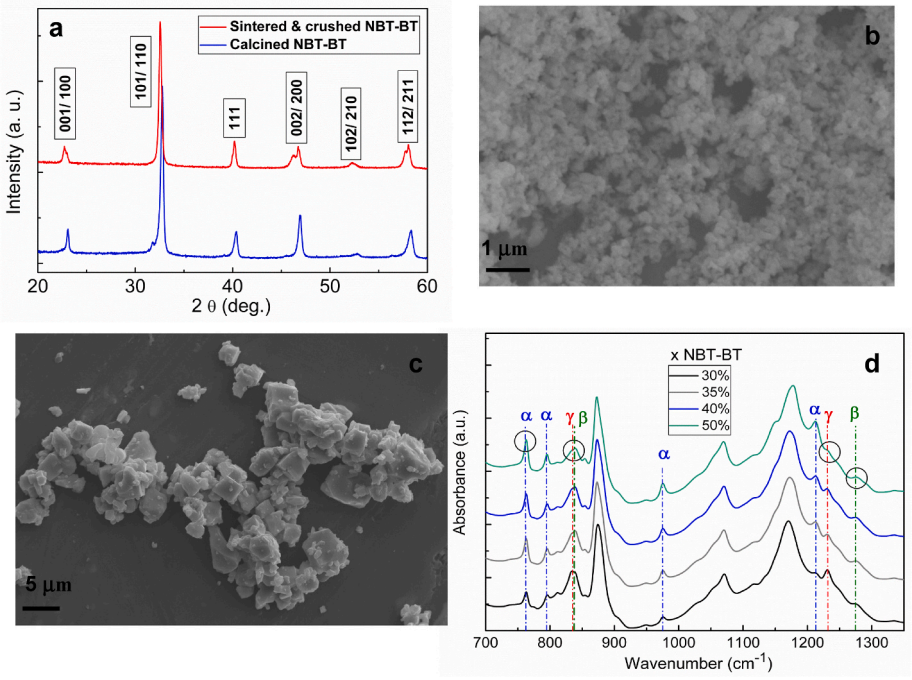

Fig. 2. a) XRD pattern of calcined and sintered & crushed NBT-BT powder b) SEM image of calcined NBT-BT powder; c) SEM image of sintered & crushed NBT-BT powder; d) FTIR spectra of composite film samples with various filler content.

In our previous paper [13], pure PVDF films prepared from polymer powder by hot pressing have been also investigated, in order to estimate the influence of hot pressing on the PVDF matrix in composites. As discussed in Ref. [13], the PVDF powder mainly consisted of the α-phase, while the hot-pressed film showed also the presence of electroactive (EA) β- and γ-phases. We recall that also PVDF films obtained by stretching show the presence of both the EA β- and γ-phases and the non-EA α-phase. Thus we concluded that a mix of polymeric phases could be present in the hot-pressed composite films. The different composite films have been further analyzed by FTIR spectroscopy to detect this polymorphism [15] and the relative phase proportion. The measurements have been carried out on both unpoled and poled samples, in order to identify possible modifications induced by the poling process on the phase content of composites. At least three measurements for each sample were performed by recording the spectra in the range 4000-400 cm^{-1}. The ATR-FTIR analysis (Fig. 2 d) evidences that the β- and γ- EA phases are present in all of the composites, displaying intensities which depend on composition (the broad band around 525 cm^{-1} is related to the stretching vibrations of metal-oxygen bond in NBT-BT; its intensity increases with the NBT-BT content). The relative fraction of the electroactive phase(s) (F_{EA}) was determined on normalized spectra [12,15] by applying the equation:

$$F_{EA} = \frac{I_{EA}}{\frac{K_{840}}{K_{763}} I_{763} + I_{EA}} \quad (1)$$

where I_{EA} is the absorbance of the band at about 840 cm^{-1} that can be assigned to β and/or γ phase, I_{763} is the absorbance of a characteristic band of the α phase at 763 cm^{-1}, and K_{840} and K_{763} are the absorption coefficients whose values, at the corresponding wavenumbers, are 7.7×10^4 and 6.1×10^4 cm^2/mol. The F_{EA} value expresses the amount of electroactive polymorphs with respect to the total crystalline phase(s) present in a given sample. In order to distinguish the contribution of β (F_β) and γ (F_γ) phase, when they are present simultaneously, the peak-to-valley height ratio between the two peaks around 1275 and 1234 cm^{-1} was considered. The ATR-FTIR spectrum corresponding to neat filler was subtracted from the spectra of the composite material.

The crystallinity degree, evaluated by differential scanning calorimetry and reported in the first column in Table S1 (Supplementary), is not significantly different across the various compositions (in the 47–50% range). The electroactive phase content, F_β/F_γ, is reported in Table S1, for both poled and unpoled samples.

It seems that the highest amount (63%) of electroactive phase is found in the NBT-BT/PVDF 30 sample, which contains only γ phase. The electroactive phase content gradually decreases down to 42% when the NBT-BT content increases to 50 vol%. However, for NBT-BT/PVDF 50 this is exclusively formed by the β phase, which is more electroactive than the γ phase. There is a relative increase of EA phase content for all the compositions after poling. Also the relative contribution of β and γ phases changes with composition and as a consequence of poling.

It must be mentioned that ATR-FTIR measurements have been performed also on as-purchased PVDF Alfa Aesar powders, and compared with those performed on hot-pressed PVDF powders. The as-purchased PVDF powders are characterized by a strong predominance of the α phase. The hot-pressing process increases the electroactive phase amount (54%), leading to a high amount of γ phase (β phase is present, but in low quantity).

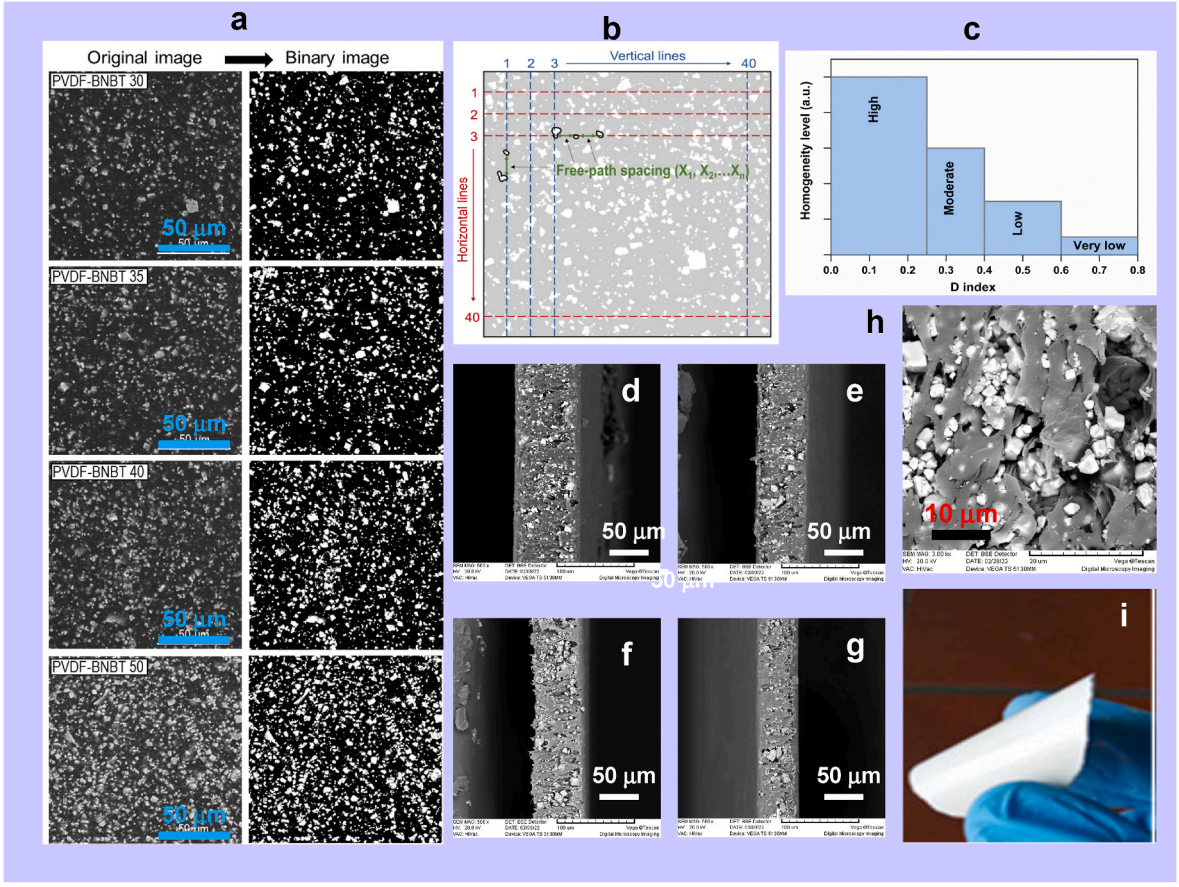

Fig. 3. a) Original SEM images and their converted binary images for NBT-BT/PVDF composite films; b) Sketch of the image analysis proposed in Ref. [22]; c) classification of the homogeneity levels for composites based on D index ranges; d)-g) Cross-section SEM images of cryo-fractured NBT-BT/PVDF 30, 35, 40 and 50 samples, respectively; h) enlarged cross-section image of NBT-BT/PVDF 35 sample; i) a typical flexible NBT-BT/PVDF composite film.

3.2. Microstructural image analysis of NBT-BT/PVDF composite films

Image analysis was made for characterizing the homogeneity of filler particles distribution in NBT-BT/PVDF composite films, following the method proposed in Ref. [22]. After converting the SEM images to binary (i.e. B/W) format (Fig. 3 a) using the ImageJ software, the free-path spacing values X_i, (i = 1, ..n) between the nearby filler particles have been evaluated and the arithmetic mean (X_m) and the standard deviation (s) have been calculated on a total of 40 lines drawn both in the horizontal and vertical direction. The distribution index (D index), which is the ratio between s and X_m, was then calculated for each composite. The degree of homogeneity for composites is illustrated in Fig. 3 c. Four classes of homogeneity levels are identified, based on the values of D index: high (for $D < 0.25$), moderate ($D < 0.40$), low ($D < 0.60$) values), and very low (for $D > 0.60$ values). The results of characterization of NBT-BT/PVDF composite films are summarized in Table S2. A moderate level of homogeneity was found for low amounts of NBT-BT particles (NBT-BT/PVDF 30 and 35), while a high homogeneity level was registered for NBT-BT/PVDF 40 and 50.

Fig. 3 d)-g) displays cross-section SEM images of cryo-fractured NBT-BT/PVDF 30, 35, 40 and 50 samples, respectively, together with an enlarged cross-section image of the NBT-BT/PVDF 35 sample (Fig. 3 h), where aggregates of micrometer particles are chained across the film thickness, sometimes almost traversing the film along the thickness. Notwithstanding, the films remained flexible and resistant, as can be seen in Fig. 3 i) for a typical NBT-BT/PVDF composite sample.

We will dwell further on this aspect when the electrical and mechanical properties will be discussed.

3.3. Dielectric relaxation spectroscopy results

Fig. 4 a) shows the variation of the real part of permittivity and of the dielectric tangent loss with temperature for the NBT-BT/PVDF 50 composite film, measured at five different frequencies from 0.2 Hz to 200 kHz. For the other samples a similar dependence was observed, except for the value of the dielectric constant in the "plateau" region around room temperature, as can be better seen in Fig. 4 c) which displays the frequency dependence of dielectric constant and loss at room temperature, measured on all the samples.

In the imaginary part of dielectric permittivity of PVDF polymer, two peaks due to relaxation processes are usually identified, corresponding to the polymer transitions [23]. As the temperature is increased, the relaxation peaks shift to higher frequency. This is observed also in NBT-BT/PVDF composites, as evidenced in Fig. 4 a (bottom plot), at least for the lower temperature peak, which corresponds to glass transition. The higher temperature peak is covered by the strong increase of dielectric permittivity, especially at lower frequencies, due to conductivity. Indeed, in dielectric systems with finite conductivity the permittivity increasing at low frequencies is related to the electrode polarization which can cover the relaxation peak. In order to evidence the low frequency dielectric relaxation, one should use the electric modulus instead of dielectric permittivity [24]. The complex electric modulus is the inverse of the complex dielectric permittivity and its real and imaginary parts, M' and M'', are defined by the equations

$$M' = \frac{\varepsilon'}{\varepsilon'^2 + \varepsilon'^2}, M' = \frac{\varepsilon'}{\varepsilon' 2 + \varepsilon'^2} \quad (2)$$

where ε' and ε'' are the real and the imaginary parts of dielectric permittivity.

Fig. 4 b) shows the imaginary part of electrical modulus vs. temperature measured on the NBT-BT/PVDF 50 composite film at different frequencies. The plot evidences two relaxation processes. The peak at lower temperature is due to the glass transition of PVDF, usually called β_a -relaxation [23,25]. It shifts to higher frequency with increasing temperature.

By analyzing the temperature dependence of these peaks, i.e. by

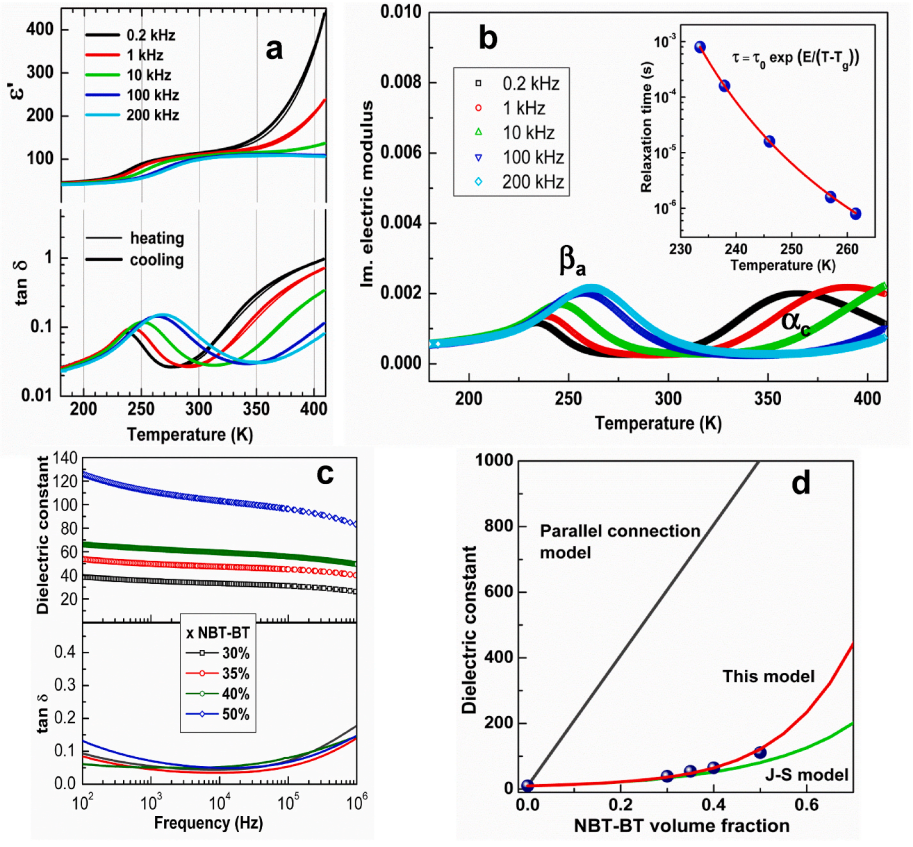

Fig. 4. a) Real part of dielectric permittivity (dielectric constant) and dielectric tangent loss variation with temperature, for different frequencies, for the NBT-BT/PVDF 50 composite film; b) Imaginary part of electrical modulus vs. temperature measured at different frequencies on the NBT-BT/PVDF 50 composite film. The inset shows the Vogel-Fulcher type dependence of the relaxation time on temperature; c) Room-temperature frequency dependence of dielectric constant and dielectric tangent loss for composite films with different NBT-BT content; d) Fitting of the measured dielectric constant dependence on the NBT-BT content with the model proposed in this work; calculations made with other models, as discussed in the text, are also shown.

plotting the inverse of radial frequency (relaxation time) versus temperature corresponding to the maximum of electrical modulus, it is found that the relaxation times follow the typical Vogel-Fulcher (V–F) behavior [25],

$$\tau = \tau_0 e^{\frac{E}{T-T_g}} \quad (4)$$

where τ_0 is the relaxation time at very high temperature, E is the activation energy and T_g is the glass transition temperature, where all the motions of the amorphous chains are frozen. The curve obtained by fitting the experimental points τ (T) with the function described by Eq. (2) is represented in Fig. 4 b (inset). The curvature of the dependence is related to the cooperative behavior associated with the V–F law. The parameters obtained by fitting are the following: E = 0.069 eV, T_g = 191.3 K, $\tau_0 = 6.5 \times 10^{-11}$ s. These values are rather similar to those reported for PVDF [25], indicating that the main interactions in composites and polymer are similar.

The relaxation peak at high temperature in Fig. 4 b) is identified as fast crystalline relaxation and is denoted as α_c –relaxation; it shifts rapidly to higher frequencies when the temperature is increased. The origin of this high temperature relaxation is related to the dynamics of the polymer crystalline lamellas [25]. In our experiment, the temperature limit of the polymer and the frequency limit of the measurement do not allow to obtain a complete view of αc –relaxation. Therefore, we could not calculate the activation energy for the crystalline relaxation since we see only the shifting of the peak up to 1 kHz in our experimental window. However information reported in literature [26] show that the relaxation follows an Arrhenius dependence and give the activation energy for the crystalline relaxation in PVDF and PVDF/$BaTiO_3$ composites to be ~0.4 eV, which is much higher than for β_a-relaxation.

In Fig. 4 c) the dielectric constant (ε') and dielectric loss tangent (tan δ) of NBT-BT/PVDF composite films with different NBT-BT content as a function of frequency are displayed at room temperature. As expected, the dielectric constant of NBT-BT/PVDF composites increases with the increase in NBT-BT content. A strong increase (nearly ten times) of the dielectric constant value at 1 kHz is observed for the sample with 50 vol % NBT-BT as compared with PVDF. The variation of ε' with NBT-BT content is displayed in Fig. 4 d) and it will be discussed in the following.

3.4. Modelling the dielectric permittivity of composite films

The present model is based on the Jayasundere-Smith (J-S) model which has been proposed in Ref. 27. In the light of this model, the NBT-BT/PVDF composite is approximated by an ensemble of spherical ceramic dielectric particles (with dielectric constant ε_c) which are homogeneously distributed in the PVDF polymer matrix (with dielectric constant ε_p). The volume fractions of the two components are x_c and x_p, respectively ($x_p + x_c = 1$). With the approximation $\varepsilon_c \gg \varepsilon_p$, the J-S model gives the following formula for the dielectric constant of the composite material where the dipolar interactions between the ceramic particles have been included (see Section S4 in Supplementary):

$$\varepsilon(x_c, \varepsilon_p, \varepsilon_c) = \frac{x_p\varepsilon_p + x_c\varepsilon_c\left[3\varepsilon_p/(2\varepsilon_p + \varepsilon_c)\right]\Phi(\varepsilon_c, \varepsilon_p, x_c)}{x_p + x_c\left[3\varepsilon_p/(2\varepsilon_p + \varepsilon_c)\right]\Phi(\varepsilon_c, \varepsilon_p, x_c)} \quad (5)$$

where $\Phi(\varepsilon_c, \varepsilon_p, x_c) = 1 + 3x_c(\varepsilon_c - \varepsilon_p)/(2\varepsilon_p + \varepsilon_c)$.

This equation converges to the correct values of the permittivity limits of the composite, that is $\varepsilon = \varepsilon_p$ for $x_c = 0$ and $\varepsilon = \varepsilon_c$ for $x_p = 0$.

We have tried first to use the J-S model for calculating the permittivity of the composite as a function of the ceramic filler volume fraction x_c, by considering $\varepsilon_p = 10$ and $\varepsilon_c = 2000$. The last value has been measured on dense NBT-BT ceramic samples. The results of calculations are displayed in Fig. 4 d) as a continuous green line. It can be observed that, although dipolar interaction effects between ceramic particles has been included in the J-S model [27], the results are still lower than the experimental values towards higher x_c values. However, as has also been observed for other materials [11], the connectivity rule in composite films could be more complex. Indeed, the model developed for the effective dielectric permittivity assumes true 0–3 connectivity in the composite. This is indeed the case when the size of the ceramic filler particles is small compared with the thickness of the composite. However, for composite thin films, when the average size of ceramic particles becomes comparable to the film thickness, there is a non-zero probability to find also 1–3 connectivity patterns. For this reason, models based on 0–3 connectivity assumption will underestimate the experimental values. Therefore, we have verified the possible presence of 1–3 connectivity patterns, by inspection of cross-section SEM images of composite films with different ceramic contents. As can be observed in Fig. 3 d)-g), the cross-section SEM images of cryo-fractured NBT-BT/PVDF 30, 35, 40 and 50 samples show aggregates of chained ceramic particles, almost traversing the film across its thickness. This is better seen in Fig. 3 h) which shows an enlarged cross-section image of NBT-BT/PVDF 35 sample, where aggregates with overall dimension of about 10–15 μm can be observed.

Thus a more complex connectivity model, which considers a minor fraction of the composite film being connected along the smallest dimension, has been employed. To calculate this fraction, a probability model proposed in Refs. [27,28] has been employed. Following Ref. [28], the reasoning goes as follows: consider a composite square plate with edge length L and thickness t, which is ideally divided into equal cubes with edge dimension l equal to the dimension of the average ceramic aggregates (macroparticle). Thus the sample can be seen as an ensemble of N columns, where $N = (L/l)^2$. Each column comprises $n = t/l$ cubes. The probability of a ceramic macroparticle occupying a cube is x_c, and the probability of a polymer macroparticle occupying a cube is x_p = 1- x_c. The probability of finding a column of n cubes containing m ceramic macroparticles is given by the binomial distribution

$$p_n(m) = \binom{n}{m}(x_c)^m(x_p)^{n-m} \quad (6)$$

From the equation above, the probability of a column to be totally occupied by the ceramic ($m = n$) (thus assigning the column to the 1–3 connectivity class) would be

$$p_n(n) = \binom{n}{n}(x_c)^n(x_p)^{n-n} = x_c^n \quad (7)$$

By again using the binomial distribution, the probability to find s columns (among the total N columns) with 1–3 connectivity is given by

$$p_N(s) = \binom{N}{s}(p_n)^s(1-p_n)^{N-s} \quad (8)$$

This is used to calculate the average of the volume fraction with 1–3 connectivity

$$_{13} = \frac{1}{N}\sum_s s p_N(s) = \frac{1}{N}Np_n = x_c^n \quad (9)$$

Thus by using a complex connectivity model, which assumes part of the composite in 1–3 connectivity (x_c^n) and the rest (1-x_c^n) in 0–3 connectivity, we obtain the effective permittivity ε_{eff} of the composite

$$\varepsilon_{eff} = (1 - x_c^n)\varepsilon(x_c, \varepsilon_p, \varepsilon_c) + x_c^n\varepsilon_{par} \quad (10)$$

where $\varepsilon_{par} = (1 - x_c)\varepsilon_p + x_c\varepsilon_c$ is the permittivity of the composite in 1–3 connectivity, which is calculated using the parallel connection model [29], and is represented by the black line in Fig. 4 d).

The results of calculation by using our model are displayed in Fig. 4 d) as a continuous red line. It can be observed that now the results approximate rather well the experimental values, even at higher ceramic volume fraction.

3.5. Anelastic spectroscopy results

The anelastic measurements have been made on strips cut out from composite films. The samples have been excited on their flexural modes and the Young's modulus Y was evaluated from the fundamental flexural resonance frequency given by the formula

$$f_1 = 1.028\frac{t}{L^2}\left(\frac{Y}{\rho}\right)^{1/2} \quad (11)$$

where t, L and ρ are the thickness, length and density, respectively. The elastic energy loss ($Q^{-1} = Y''/Y'$) was obtained from the width of the resonance curves. During the same temperature run, also the third flexural mode ($f_3 \cong 5.4f_1$) and higher modes have been probed. The temperature dependence of the Young's modulus can be plotted as $Y/Y_0 = (f/f_n)^2$, with the absolute value Y_0 given by Eq. (11) for $n = 1$, neglecting the temperature dependence of the sample dimensions with respect to that of Y. The resonance frequencies decrease of nearly four times from the highest to the lowest temperatures tested. Fig. 5 shows, together with a sketch of the electrostatic excitation of the composite sample (a), the temperature dependence of the Young's modulus and the elastic energy loss for the NBT-BT/PVDF 50 composite film, measured at different frequencies (b). For the other samples a similar dependence was observed, except for the magnitude of the modulus. Fig. 5 c) displays the variation of the Young's modulus at room temperature with NBT-BT content and the fitting of this dependence with the model proposed in this work, as will be discussed in the following. As can be seen in Fig. 5 b), the temperature dependence of the Young's modulus and of the mechanical losses looks like those of PVDF [25]. However, Young's modulus is larger than that of PVDF and, as shown in Fig. 5 c), it increases with the NBT-BT content. The loss peaks and the modulus steps shift to higher frequency with increasing temperature. The first loss peak, which is observed at ~240 K for the frequency of ~1 kHz, is certainly the same as that evidenced in dielectric spectroscopy measurements (Fig. 4 b). There are only a few studies of relaxation processes in composites by combined dielectric and anelastic spectroscopies [13, 25]. Indeed, the correlation between the two techniques can be useful to gain insight into the relaxation dynamics in composites. For example, in the case of NBT-BT/PVDF composites, it can be observed that the relaxation processes are the same as in PVDF. Both measurements show the amorphous phase relaxation,i. e. the β_a relaxation (first loss peak in Figs. 4 b and Fig. 5 b) and the α_c-relaxation related to the molecular dynamics in the crystalline phase (second loss peak in Figs. 4 b and Fig. 5 b). If this is true, one must think of the hot-pressing process used to obtain the ceramic-polymer composite films as similar, at least in some aspects, to the usual stretching process imparted to change the phase in PVDF preparation. Indeed, stretching of the α-PVDF samples produces changes of the crystalline phase content, by melting of the α-PVDF amorphous phase under the applied stress, followed by recrystallization in the β crystalline phase. This reorganization process produced by the high deformation is not complete and affects only a part of the α crystals both in the stretching and hot-pressing procedures, although it is better and less polymorphic (minor content of γ phase) for the first method. The β_a-relaxation process, evidenced in both dielectric and mechanical relaxation spectra, is related to the correlated movements of the amorphous segments and to the glass transition dynamics of PVDF [25]. As previously stated for the dielectric loss, the relaxation peak at about 350 K in Fig. 5 b) is identified as fast crystalline relaxation and is denoted as α_c – relaxation. The origin of this high temperature relaxation is related to the molecular motions in the crystalline phase of PVDF [25].

The variation of the Young's modulus of the composites with NBT-BT content, shown in Fig. 5 c), has been fitted first with a model proposed by Furukawa et a. in Ref. [30]. The Furukawa (F) model is based on the assumption that the component phases in the composite are incompressible. Moreover, it is assumed that the materials are characterized by two elastic constants, namely bulk and shear moduli. In these conditions, the following expression was found in Ref. [30] for the Young's modulus of the composite, Y:

$$Y(x_c, Y_p, Y_c) = \frac{3Y_p + 2Y_c - 3x_c(Y_p - Y_c)}{3Y_p + 2Y_c + 2x_c(Y_p - Y_c)} \quad (12)$$

where Y_p and Y_c are the Young's moduli of PVDF polymer and NBT-BT ceramic, respectively.

By using Eq. (12) with the Young's modulus values for the NBT-BT ceramic (~100 GPa) and polymer (2.45 GPa), the Young's modulus values of the composite films are calculated and plotted as the green curve in Fig. 5 c). It can be observed that the calculated values underestimate the experimental values, especially at high ceramic content.

Therefore we propose a new model, which is based on Furukawa model. As previously done for the dielectric permittivity, the presence of a fraction x_c^n in 1–3 connectivity is considered and the effective Young's modulus of the composite is obtained by considering the 0–3 and 1–3 connectivity fractions as separate media in parallel connection

$$Y_{eff} = (1 - x_c^n)\,Y(x_c, Y_p, Y_c) + x_c^n Y_{par} \quad (13)$$

where $Y_{par} = (1 - x_c)Y_p + x_c Y_c$ is the Young's modulus of the composite in 1–3 connectivity, which is calculated by the parallel connection model, based on the assumption that the strain inside the composite is uniform [31], and it is represented by the black line in Fig. 5 c).

The results of calculation are displayed in Fig. 5 c) as continuous pink line. It can be observed that now the results approximate the experimental values better, even at higher ceramic volume fraction.

3.6. Piezoelectric response to ultrasonic signal

High piezoelectric response at MHz frequencies is necessary for ultrasound wireless-powered devices. The piezoelectric response at ultrasound frequencies has been evaluated by piezoelectric probe measurements [19]. In Fig. 6 a) a picture of the measurement setup is

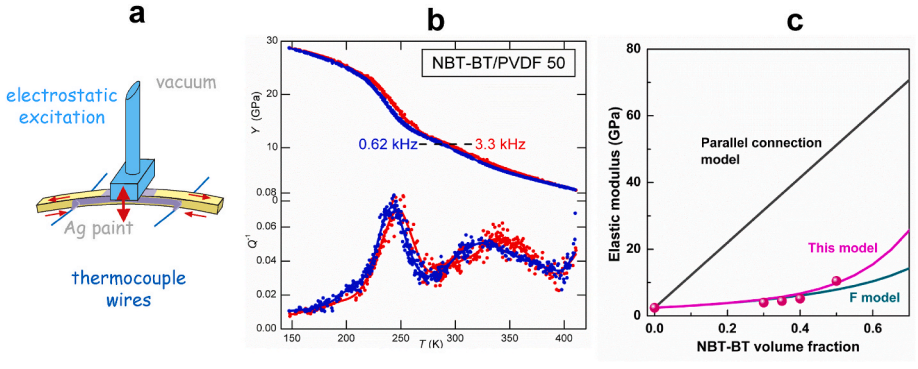

Fig. 5. a) Sketch of the electrostatic excitation (double red arrow) of free flexural resonance in the composite sample; the red arrows show the uniaxial deformation, non-uniform across the sample thickness, through which the Young's modulus is probed; b) temperature dependence of the Young's modulus and the mechanical losses for the NBT-BT/PVDF 50 composite film, measured exciting the 1st and 3rd flexural modes, resonating at 0.62 and 3.3 kHz at room temperature, respectively; c) Fitting of the room temperature Young's modulus dependence on the NBT-BT content with the model proposed in this work. Calculations made with other models, as discussed in the text, are also shown. (For interpretation of the references to colour in this figure legend, the reader is referred to the Web version of this article.)

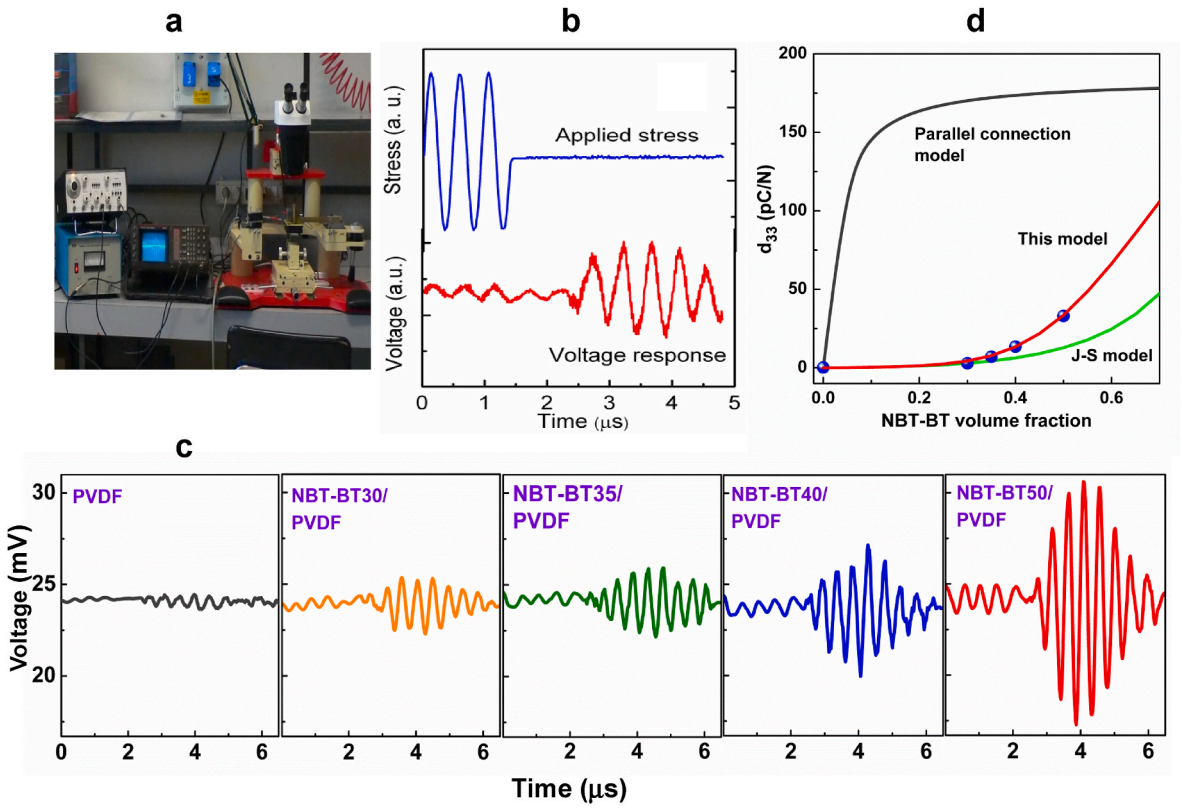

Fig. 6. a) A picture of the piezoelectric probe measurement set up; b) applied ultrasound signal by the piezoelectric probe and piezoelectric response of a composite film; c) piezoelectric response of composite films with different NBT-BT content; d) fitting of d_{33} dependence on the NBT-BT content with the model proposed in this work; calculations made with other models, as discussed in the text, are also shown.

shown. The probe itself consists of a piezoelectric plate bonded on the upper end of a metallic rod. The piezoelectric plate is driven at its resonant frequency (~2 MHz) and generates, through piezoelectric effect, an ultrasound wave which propagates inside the rod. The lower end of the rod, which has the shape of a truncated cone terminating with a small flat tip (~1 mm diameter), is gently pressed on the sample surface, through a water droplet. The piezoelectric probe is assembled in a mechanical system supporting a fine three-axial positioning stage that allows its movement parallel to the surface of the sample to be tested, as well as along the normal to the surface. The voltage generated by the transfer of ultrasound energy in the stressed region is measured by an oscilloscope. The ultrasound wave generated by the piezoelectric plate arrives at the end tip of the rod with a delay time of about 2 μs with respect to the electrical driving signal. Therefore, the piezoelectric response signal from the composite film, measured by the oscilloscope, has the same delay with respect to the applied electrical signal on the transducer generating the ultrasound signal. This is observed in Fig. 6 b) where both the applied electric signal to the probe and the output voltage signal in the composite film are displayed. The output voltage of the films has the same frequency as the exciting signal (2 MHz, or a time period of 0.5 μs). Moreover, the generated electrical signals are reversed when the electrodes contacts are inverted, indicating a true piezoelectric signal response in the composite film. Taking into account that the piezoelectric composite films have a thickness resonant frequency of ~12 MHz (see Fig. S1), this resonance cannot be excited by the driving ultrasound signal, thus the composite films work outside resonance. Nonetheless, the samples show a good piezoelectric response, which is progressively increasing with the content of NBT-BT phase (Fig. 6 c). The apparent difference among the output voltages displayed in Fig. 6b) and c) and the output voltages obtained in Refs. [16–18] is due to the initial delay time (as explained above) and to the burst type of excitation. Indeed, the driving signal consists of ultrasound bursts of a few microseconds, in order to increase the signal-to-noise ratio. The burst duration and repetition rate are carefully chosen in order to avoid overlapping with unwanted parasitic signals. The obtained output voltage curve is a proper signal response of piezoelectric composites to the ultrasound bursts.

The information about the efficiency of the piezoelectric material is given by the relative amplitude of the output signal. In order to calculate the piezoelectric constant, a reference sample like a thin $LiNbO_3$ single-crystal plate is tested in the same experimental conditions, and the output signal is compared with that measured on the composite film.

Fig. 6 d) displays the measured piezoelectric constant, d_{33}, as a function of the NBT-BT content. The fitting of this dependence with various models will be discussed in the next section.

The AC electric signal harvested at ultrasonic frequencies can be converted to DC power supply voltage by using a rectifying bridge connected in parallel to a filter capacitance.

Using the equation relating the electrical energy U to the capacitance C and voltage V, $U = \frac{1}{2}CV^2$ and the constitutive piezoelectric equations, a simple relationship can be derived between the harvested energy density u and the applied stress σ: $u = \frac{1}{2}dg\sigma^2$, where d is the piezoelectric strain constant and g is the piezoelectric voltage constant ($g = d/\varepsilon$). Thus the electrical energy density which is harvested from an ac stress field is directly dependent on the product $d{\cdot}g$, therefore called figure of merit (FOM), as previously stated.

In our case, taking the example of NBT-BT/PVDF 50 composite film, with $d_{33} \cong$ 33 pC/N and $g_{33} \cong$ 46.6 mV m/N, the figure of merit is: $d_{33}g_{33} \cong 1.54 \times 10^{-12}$ m^3/J, which is comparable to the figure of merit for the NBT-BT piezoelectric ceramic (1.8×10^{-12} m^3/J). Thus a high electrical energy density is harvested from the ultrasound wave by the NBT-BT/PVDF 50 composite film.

A comparison with other results obtained on different composites and reported in the literature is given in Table 1. It can be observed that

Table 1
Comparison of dielectric and piezoelectric properties, including the figure of merit $d_{33}g_{33}$, obtained on different random piezoelectric ceramic/polymer composites with comparable filler fraction.

Composite	Filler vol%	ε' (@ 1 kHz)	tan δ	d_{33} (pC/N)	g_{33} (mV m/N)	d_{33} g_{33} (10^{-12} m^3/J)	Ref.
NBT-BT/PVDF	40	65	0.04	13.5[a)]	30.5[a)]	0.41[a)]	This work
NBT-BT/PVDF	50	111	0.07	33[a)]	46.6[a)]	1.54[a)]	This work
BFO/PVDF	50	75		26	40	1.04	[32]
PZT/PVDF	48	59.1	0.032	22[b)]	42[b)]	0.924[b)]	[9]
BTO/PVDF	45	70	0.025	22	35.5	0.781	[33]
KNLN/PU[c)]	50	37	0.04	15	45.8	0.687	[34]
KBT/PVDF	50	69.7[d)]	0.44[d)]	20	32.75	0.655	[35]
PZT/PVDF	50	80	0.03	16	30	0.48	[36]

a) @ 2 MHz; b) Values for d_{31} and g_{31}; c) PU = polyurethane; d) @ 1 MHz.

for the NBT-BT/PVDF 50 composite we have obtained superior dielectric constant, d_{33} piezoelectric constant and $d_{33}g_{33}$ figure of merit.

3.7. Modelling the piezoelectric response of composite films

The proposed model is based on the Jayasundere-Smith (J-S) model for random piezoelectric ceramic-polymer composites which has been developed in Ref. [37], with the assumptions that the piezoelectric constant of the polymer is negligible and the dielectric constant of ceramic is much higher than that of polymer. The J-S model gives the following formula for the piezoelectric constant of the composite material (see Section S4 in Supplementary material):

$$d_{33}\left(x_c, d_{33}^c, \varepsilon_c, \varepsilon_p, Y_c, Y_p\right) = d_{33}^c \frac{Y_c}{Y} \frac{Y - Y_p}{Y_c - Y_p} \frac{\varepsilon}{\varepsilon_c}\left(1 + \frac{3x_c\varepsilon_c}{2\varepsilon_p + \varepsilon_c}\right) \tag{14}$$

By using this formula, with the dielectric permittivity and Young's modulus values specified in the previous sections, and assuming $d_{33}^c \sim$ 180 pC/N, the piezoelectric constants of the composite films for different x_c values are calculated and plotted as the green curve in Fig. 6 d). It can be observed that the calculated values are lower than the experimental values, especially at high ceramic content.

Therefore we propose a new model, which is based on J-S model. As previously done for the dielectric permittivity and Young's modulus, the presence of a fraction x_c^n in 1–3 connectivity is considered and the effective piezoelectric constant of the composite films is obtained by considering the 0–3 and 1–3 connectivity fractions as separate media in parallel connection

$$d_{33}^{eff} = \frac{\left(1 - x_c^n\right) d_{33} / Y_{par} + x_c^n d_{33}^{par} / Y}{\left(1 - x_c^n\right) / Y_{par} + x_c^n / Y} \tag{15}$$

where $d_{33} = d_{33}(x_c, d_{33}^c, \varepsilon_c, \varepsilon_p, Y_c, Y_p)$ from (Eq. (14)) corresponds to the 0–3 connectivity composite fraction and d_{33}^{par} is the piezoelectric constant of the composite fraction in 1–3 connectivity (recall that the d_{33} contribution of the polymer is neglected),

$$d_{33}^{par} = \frac{x_c d_{33}^c / Y_p}{\left(1 - x_c\right) / Y_c + x_c / Y_p} \tag{16}$$

which is calculated using the parallel connection model [29], and is represented by the black line in Fig. 6 d). The results of calculation with Eq. (15) are displayed in Fig. 6 d) as a continuous red line. It can be observed that now the calculated values are quite similar to the experimental values, even at higher ceramic volume fraction.

It is now time to discuss the problem of poling operation of ferroelectric ceramic-polymer composites, which was postponed in the previous sections. It has often been mentioned that low piezoelectric performance in piezoelectric composites could be due to insufficient poling of the ceramic particles inside the composite. Indeed, this is plausible since the electric field on the ceramic particles (as obtained from the electrical boundary conditions at the ceramic-polymer interface) is only a tiny fraction $(\varepsilon_p / \varepsilon_c)E_0$ of the applied electric field E_0 on the composite film, which would be clearly insufficient for poling. However, the results obtained from measurements of d_{33} show that the experimental values correspond to the expected values, calculated with the assumption that the piezoelectric ceramic particles are fully poled (Fig. 6 d). As shown in Ref. [38], adopting long poling times in the production process of composites is equally important as using high values of the applied electric field at high temperatures. The explanation is that, during the poling operation, the small instantaneous internal electric field of the ceramic increases in time, eventually overcoming the value of coercive field, due to charge accumulation at the boundaries related to the DC conductivity in the polymer. We remind the reader that poling of our samples was performed under a 50 kV/cm electric field in a silicon bath at 135 °C for 40 min, which was obviously sufficient to fully polarize the ceramic particles.

4. Conclusions

In summary, a series of flexible lead-free NBT-BT/PVDF piezocomposites with variable filler content up to 50 vol% have been prepared by hot pressing, by incorporating in a complex connectivity pattern fully sintered NBT-BT crystalline powders in the PVDF matrix. The composites display enhanced high frequency piezoelectric properties which make them very attractive for wireless ultrasound-powered medical implants. The relative dielectric constant of the flexible composites increased from 10 of pure PVDF polymer to 110 of composite films with 50 vol% NBT-BT content, while the piezoelectric d_{33} constant increased from 0.2 pC/N to 33 pC/N for the same samples, at ultrasound frequencies. We further proposed a model which takes into account the complex connectivity of filler phase in order to explain the enhanced dielectric permittivity, elastic modulus and piezoelectric coefficients. Moreover, the NBT-BT/PVDF composite with 50 vol% NBT-BT exhibits the figure of merit for the harvested ultrasound energy $d_{33}g_{33} \cong 1.54 \times 10^{-12}$ m^3/J, which is comparable to the figure of merit for the NBT-BT piezoelectric ceramic (1.8×10^{-12} m^3/J). Therefore, along with the results, this study provides an attractive strategy to fabricate random flexible piezoelectric composites with enhanced high frequency piezoelectric response and high energy density harvested from an ultrasound source.

CRediT authorship contribution statement

Floriana Craciun: Conceptualization, Writing – original draft, Writing – review and editing, Investigation, Project administration, Supervision. **Francesco Cordero:** Investigation, Data analysis, Writing – review and editing. **Elisa Mercadelli:** Methodology, Investigation, Data analysis, Writing – review and editing. **Nikola Ilic:** Investigation, Methodology. **Carmen Galassi:** Conceptualization, Writing – review and editing. **Carlo Baldisserri:** Methodology, Validation, Writing – review and editing. **Jelena Bobic:** Methodology, Data analysis. **Paola Stagnaro:** Conceptualization, Resources, Investigation, Writing – review and editing. **Giovanna Canu:** Methodology, Investigation, Writing – review and editing. **Maria Teresa Buscaglia:** Methodology, Investigation, Writing – review and editing. **Adis Dzunuzovic:** Investigation, Methodology. **Mirjana Vijatovic Petrovic:** Investigation, Data analysis, Writing – review & editing, Project administration, Supervision.

Declaration of competing interest

The authors declare that they have no known competing financial

interests or personal relationships that could have appeared to influence the work reported in this paper.

Data availability

Data will be made available on request.

Acknowledgements

The authors gratefully acknowledge the bilateral project "Lead-free piezoelectric and multiferroic flexible films for nanoelectronics and energy harvesting" between the Italian Ministry of Foreign Affairs and International Cooperation and the Serbian Ministry of Education, Science and Technological Development (Project code: RS19MO01). Claudio Capiani from CNR-ISSMC (for the preparation of the NBT-BT powders) and Paolo Massimiliano Latino from CNR-ISM (for technical assistance) are gratefully acknowledged.

Appendix A. Supplementary data

Supplementary data to this article can be found online at https://doi.org/10.1016/j.compositesb.2023.110835.

References

[1] Jiang L, Yang Y, Chen Y, Zhou Q. Nano Energy 2020;77:105131.
[2] Liang L, Sun C, Zhang R, Han S, Wang J, Ren N, Liu H. Nano Energy 2021;90:106634.
[3] Chen P, Wu P, Wan X, Wang Q, Xu C, Yang M, Feng J, Hu B, Luo Z. Nano Energy 2021;86:106123.
[4] Shi X, Chen Y, Zhao Y, Ye M, Zhang S, Gong S. Biomater Sci 2022;10:692.
[5] Uchino K. Piezoelectric composite materials. In: Uchino K, editor. Advanced piezoelectric materials: science and technology. Duxford, UK: Woodhead Publishing (Elsevier); 2017. p. 353–84. https://doi.org/10.1016/B978-0-08-102135-4.00009-6 [chapter 9].
[6] Bouhamed A, Binyu Q, Böhm B, Jöhrmann N, Behme N, Goedel WA, Wunderle B, Hellwig O, Kanoun O. Compos Sci Technol 2021;208:108769.
[7] Guo J, Fu P, Qiu Z, Chen C, Wang a S, Zhang K, et al. Compos Sci Technol 2021;209:108796.
[8] Sonoda K, Juuti J, Moriya Y, Jantunen H. Compos Struct 2010;92:1052–8.
[9] Siponkoski TK, Jantunen HM, Juuti JA. Appl Phys Lett 2022;120:052903.
[10] Hilczer B, Kułek J, Markiewicz E, Kosec M, Malic B. J Non-Cryst Solids 2002;305:167–73.
[11] Pardo L, Mendiola J, Alemany C. J Appl Phys 1988;64:5092.
[12] Brunengo E, Conzatti L, Schizzi I, Buscaglia MT, Canu G, Curecheriu L, Costa C, Castellano M, Mitoseriu L, Stagnaro P, Buscaglia V. J Appl Polym Sci 2020:e50049.
[13] Vijatovic Petrovic M, Cordero F, Mercadelli E, Brunengo E, Ilic N, Galassi C, Despotovic Z, Bobic J, Dzunuzovic A, Stagnaro P, Canu G, Craciun F. J Alloys Compd 2021;884:161071.
[14] Buscaglia V, Randall CA. J Eur Ceram Soc 2020;40:3744–58.
[15] Brunengo E, Luciano G, Canu G, Canetti M, Conzatti L, Castellano M, Stagnaro P. Polymer 2020;193:122345.
[16] Ponnamma D, Parangusan H, Tanvir A, Al-Maadeed MA. Mater Des 2019;184:108176.
[17] Yea S, Cheng C, Chen X, Chen X, Shao J, Zhang J, Hu H, Tian H, Li X, Ma L, Jia W. Nano Energy 2019;60:701–14.
[18] Zhou X, Parida K, Halevi O, Liu Y, Xiong J, Magdassi S, Lee PS. Nano Energy 2020;72:104676.
[19] Verardi P, Craciun F. Rev Sci Instrum 2003;74:4453.
[20] Cordero F, Dalla Bella L, Corvasce F, Latino PM, Morbidini A. Meas Sci Technol 2009;20:015702.
[21] Cordero F, Craciun F, Trequattrini F, Mercadelli E, Galassi C. Phys Rev B 2010;81:144124.
[22] Yakaboylu GA, Sabolsky EM. J Microsc 2017;266:263–72.
[23] Bello A, Laredo E, Grimau M. Phys Rev B 1999;60:12764.
[24] Hodge IM, Ngai KL, Moynihan CT. J Non-Cryst Solids 2005;351:104–15.
[25] Sencadas V, Lanceros-Mendez S, Sabater i Serra R, Andrio Balado A, Gomez Ribelles JL. Eur Phys J E 2012;35:41.
[26] Chanmal CV, Jog JP. Express Polym Lett 2008;2:294–301.
[27] Jayasundere N, Smith BV. J Appl Phys 1993;73:2462.
[28] Gerson R, Marshall TC. J Appl Phys 1959;30:1650.
[29] Skinner DP, Newnham RE, Cross LE. Mater Res Bull 1978;13:599–607.
[30] Furukawa T, Fujino K, Fukada E. Jap. J. Appl. Phys. 1976;15:2119–29.
[31] Hill R. J Mech Phys Solid 1963;11:357–72.
[32] Tuluk A, Mahon T, van der Zwaag S, Groen P. J Alloys Compd 2021;868:159186.
[33] Dalle Vacche S, Oliveira F, Leterrier Y, Michaud V, Damjanovic D, Manson J-AE. J Mater Sci 2012;47:4763–74.
[34] Stuber VL, Mahon TR, van der Zwaag S, Groen P. Mater Res Express 2020;7:015703.
[35] Dwivedi S, Badole M, Pareek T, Kumar S. J Alloys Compd 2021;871:159616.
[36] Li R, Zhou J, Liu H, Pei J. Materials 2017;10:945. https://doi.org/10.3390/ma10080945.
[37] Jayasundere N, Smith BV, Dunn JR. J Appl Phys 1994;76:2993.
[38] Furukawa T, Suzuki K, Date M. Ferroelectrics 1986;68:33–44.